

Binary neutron star merger simulations with hot microscopic equations of state

A. Figura¹, Fan Li (李凡)², Jia-Jing Lu (陆家靖)², G. F. Burgio¹, Zeng-Hua Li (李增花)², and H.-J. Schulze¹

¹ *INFN Sezione di Catania, Dipartimento di Fisica, Università di Catania, Via Santa Sofia 64, 95123 Catania, Italy*

² *Institute of Modern Physics, Key Laboratory of Nuclear Physics and Ion-beam Application (MOE), Fudan University, Shanghai 200433, P.R. China*

(Dated: January 5, 2022)

We perform binary neutron star merger simulations using a newly derived set of finite-temperature equations of state in the Brueckner-Hartree-Fock approach. We point out the important and opposite roles of finite temperature and rotation for stellar stability and systematically investigate the gravitational-wave properties, matter distribution, and ejecta properties in the postmerger phase for the different cases. The validity of several universal relations is also examined and the most suitable EOSs are identified.

I. INTRODUCTION

After the first detection of gravitational waves (GWs) from a binary neutron star merger (BNSM) [1], and its related electromagnetic counterparts [2], the constraints on the equation of state (EOS) governing nuclear matter in neutron stars (NSs) have been impressively refined [3–8]. In particular, GWs from the inspiral phase have already set constraints on the EOS at zero temperature, showing consistency with small neutron star radii and tidal deformabilities [9]. The future detection of a post-merger GW signal could instead provide information on the EOS of hot (with temperatures of typically several tens of MeVs [10, 11]) and dense (a few times nuclear saturation density $\rho_0 \sim 2.7 \times 10^{14} \text{ g/cm}^3$) nuclear matter: interestingly, such signal could also be indicative of the appearance of deconfined quark matter [12–15]. Due to the frenetic theoretical activity in this field, the relevant literature is vast and we refer to recent reviews [16, 17] for an overview.

The accurate simulation of BNSMs represents in this context a necessary tool to analyze both the GW signal and the hydrodynamic properties involved in these phenomena, and the use of a constraint-fulfilling, realistic EOS is an essential requirement. Such an EOS should cover [18] a typical range of about $10^4 < \rho < 10^{15} \text{ g/cm}^3$ in rest-mass densities and $0 \leq T \lesssim 100 \text{ MeV}$ in temperatures, and should be computed without postulating beta-equilibrium, accounting for electron fractions in a typical range $0 \leq Y_e \leq 0.65$.

EOSs of this kind are very few and generally employ phenomenological models rather than ab-initio calculations; noteworthy cases are Relativistic Mean Field (RMF) models such as the Shen EOS [19], the DD2 EOS [20], the SFHo EOS [21, 22], or the BH $\Lambda\phi$ EOS [23], which also accounts for hyperon-hyperon interactions. We also mention the very commonly used LS220 EOS [24], a model based on nonrelativistic Skyrme interactions, the Togashi model [25], based on a variational approach, and the recent Chiral Mean Field (CMF) theory based EOS presented in Ref. [15], where also the possible deconfinement to quark matter is considered.

Given the restricted number of publicly available and constraint-fulfilling finite-temperature EOSs, BNSM simulations are also usually performed using the so-called “hybrid-EOS” approach [26–41], in which pressure and the specific internal energy can be expressed as the sum of a “cold” contribution, obeying a zero-temperature EOS, and of a “thermal” contribution obeying the ideal-fluid EOS (see Ref. [42] for

further details). The latter approach, however, is still far from being realistic, as a constant thermal adiabatic index Γ_{th} does not accurately describe the behavior of nuclear matter at finite temperature [11, 43].

We have introduced in Ref. [44] four state-of-the-art finite-temperature EOSs constructed in the Brueckner-Hartree-Fock (BHF) approach, which have been shown to fulfill all current constraints imposed by observational data from nuclear structure, heavy-ion collisions, NS global properties, and recently NS merger events [45, 46]. One of those EOSs, labeled V18 (see Sec. II for details), was already examined in our previous paper [11], in which the merger simulations were performed mainly employing the widely used hybrid-EOS approach. Here we discuss novel results recently obtained from merger simulations in which these four BHF finite-temperature EOSs were employed, thus overcoming the approximate hybrid-EOS approach. We find that differences observed in the simulations are strongly related to the stiffness of the adopted EOSs. We investigate both the hydrodynamic and GW properties, focusing on the stability and mass distribution of the remnant and the properties of the ejected matter. Since present GW detectors are not capable to see the post-merger phase of BNSMs, our results will serve as predictions to confront with future observations.

The article is organized as follows. We first review in Sec. II the computation of our EOSs in the BHF formalism and discuss their basic characteristics. The specific properties of the GW signal to be analyzed are introduced in Sec. III. The numerical setup and methods used in this work for BNSM simulations are introduced in Sec. IV. Results of the simulations are presented in Sec. V, and conclusions are drawn in Sec. VI.

II. EQUATION OF STATE AT FINITE TEMPERATURE

A. The microscopic BHF approach

The extension of the BHF approach to finite temperature was first formulated by Bloch & De Dominicis [47]. In the following we only provide a brief overview of the formalism for asymmetric nuclear matter, referring to the relevant references [47–55], in particular the recent [44], for further details. In this approach, the essential ingredient is the two-body in-medium scattering matrix K , which, along with the single-particle (s.p.) potential U , satisfies the self-consistent

equations

$$K(n_B, x_p; W) = V + V \operatorname{Re} \sum_{1,2} \frac{|12\rangle(1-n_1)(1-n_2)\langle 12|}{W - e_1 - e_2 + i0} K(n_B, x_p; W) \quad (1)$$

and

$$U_1(n_B, x_p) = \operatorname{Re} \sum_2 n_2 \langle 12 | K(n_B, x_p; e_1 + e_2) | 12 \rangle_a, \quad (2)$$

where $n(k)$ is a Fermi distribution, $x_p = n_p/n_B$ is the proton fraction, and n_p and n_B are the proton and the total baryon number densities, respectively. (In the following we also use the notation $\rho_i = m_N n_i$ and $\rho = m_N n_B$ for the rest-mass densities, being $m_N = 1.67 \times 10^{-24}$ g the nucleon mass). W is the starting energy and $e(k) \equiv k^2/2m + U(k)$ is the s.p. energy. The multi-indices 1,2 denote in general momentum, isospin, and spin.

Several choices for the realistic nucleon-nucleon interaction V are adopted in the present calculations: the Argonne V_{18} [56], the Bonn B (BOB) [57, 58], and the Nijmegen 93 (N93) [59, 60], and compatible three-body forces (TBF) as input. We remind the reader that in our approach the TBF are reduced to an effective two-body force and added to the bare potential V , see Refs. [45, 61–63] for details. More precisely, the BOB and N93 are supplemented with microscopic TBF employing the same meson-exchange parameters as the two-body potentials [45, 61–63], whereas V_{18} is combined either with a microscopic or a phenomenological TBF, the latter consisting of an attractive term due to two-pion exchange with excitation of an intermediate Δ resonance, and a repulsive phenomenological central term [64–67]. They are labeled as V18 and UIX, respectively, throughout the paper and in all figures.

A simplification of the Bloch & De Dominicis scheme can be achieved by disregarding the effects of finite temperature on the s.p. potential $U_{n,p}(k)$, and using the $T = 0$ results in order to speed up the calculations. This is the so-called frozen-correlations approximation, and it has been frequently used in some of our previous papers [44, 50–54]. It has been shown that at not too high temperature ($T \lesssim 30$ MeV) this produces a negligible effect on thermodynamic properties of nuclear matter [48–51, 55]. Within this approximation, the nucleonic free energy density has the following simplified expression,

$$f_N = \sum_{i=n,p} \left[2 \sum_k n_i(k) \left(\frac{k^2}{2m_i} + \frac{1}{2} U_i(k) \right) - T s_i \right], \quad (3)$$

where i denotes the nucleonic species and

$$s_i = -2 \sum_k \left(n_i(k) \ln n_i(k) + [1 - n_i(k)] \ln [1 - n_i(k)] \right) \quad (4)$$

is the entropy density treated as a free Fermi gas with spectrum $e_i(k)$. From the total free energy density $f = f_N + f_L$, including the lepton contribution f_L as a finite-temperature Fermi gas, one can compute all relevant observables in a thermodynamically consistent way. In fact one can define the chemical potentials

$$\mu_i = \frac{\partial f}{\partial n_i}, \quad (5)$$

from which the composition of metastable stellar matter can be obtained, and then the total pressure p and the internal energy density ε ,

$$p = n_B^2 \frac{\partial (f/n_B)}{\partial n_B} = \sum_i \mu_i n_i - f, \quad (6)$$

$$\varepsilon = f + T s, \quad s = -\frac{\partial f}{\partial T}. \quad (7)$$

In order to simplify the calculations employing these EOSs, in Ref. [44] we gave numerical parametrizations for the free energy density of symmetric nuclear matter (SNM) and pure neutron matter (PNM), and used a parabolic approximation for the x_p dependence of asymmetric nuclear matter [55, 68–70],

$$f(n_B, T, x_p) \approx f_{\text{SNM}}(n_B, T) + (1 - 2x_p)^2 [f_{\text{PNM}}(n_B, T) - f_{\text{SNM}}(n_B, T)]. \quad (8)$$

In Ref. [71] it has been confirmed that this is an excellent approximation for our purposes. This specifies the EOS for arbitrary values of baryon density, proton fraction, and temperature, which can then be employed for computing the mass-radius relation of cold NSs by solving the Tolman-Oppenheimer-Volkov (TOV) equations for charge-neutral metastable matter including leptons, and in the merger simulations discussed in the following sections.

We notice that, since our EOSs account only for homogeneous matter in the core region of the NS, we have to attach an EOS for the crust which takes properly into account clustered matter at lower density $\rho \lesssim 10^{14}$ g/cm³ for every value of temperature and proton fraction; for that purpose we choose the Shen EOS [19]. Furthermore, we also include in all our simulations an artificial low-density background atmosphere, $\rho \lesssim 10^3$ g/cm³, evolved as discussed in [72].

B. EOS and stellar structure

To illustrate the difference between the four EOSs regarding the bulk properties of NSs, Fig. 1 shows the NS gravitational mass vs. central density and NS radius diagrams, obtained in the standard way by solving the TOV equations for metastable and charge-neutral matter, at the two temperatures $T = 0, 50$ MeV for both static and fastest uniformly rotating (with mass-shedding frequency f_{Kepler}) configurations for the different EOSs. In the figure we also indicate by markers the baryonic masses for different configurations. The values of maximum masses and Kepler frequencies are also summarized in Table I.

Regarding the properties of the static cold NSs, the maximum masses of all EOSs except the UIX are larger than the current observational lower limit $M > 2.14_{-0.09}^{+0.10} M_\odot$ [73]. Concerning the radius, we found in [7, 8] that the values of a 1.4-solar-mass NS, $R_{1.4} = 12.97, 12.47, 12.91, 11.96$ km for BOB, V18, N93, UIX, fulfill the constraint derived from the tidal deformability in the GW170817 merger event, $R_{1.36} = 11.9 \pm 1.4$ km [9]. They are also compatible with estimates of the mass and radius of the isolated pulsar PSR

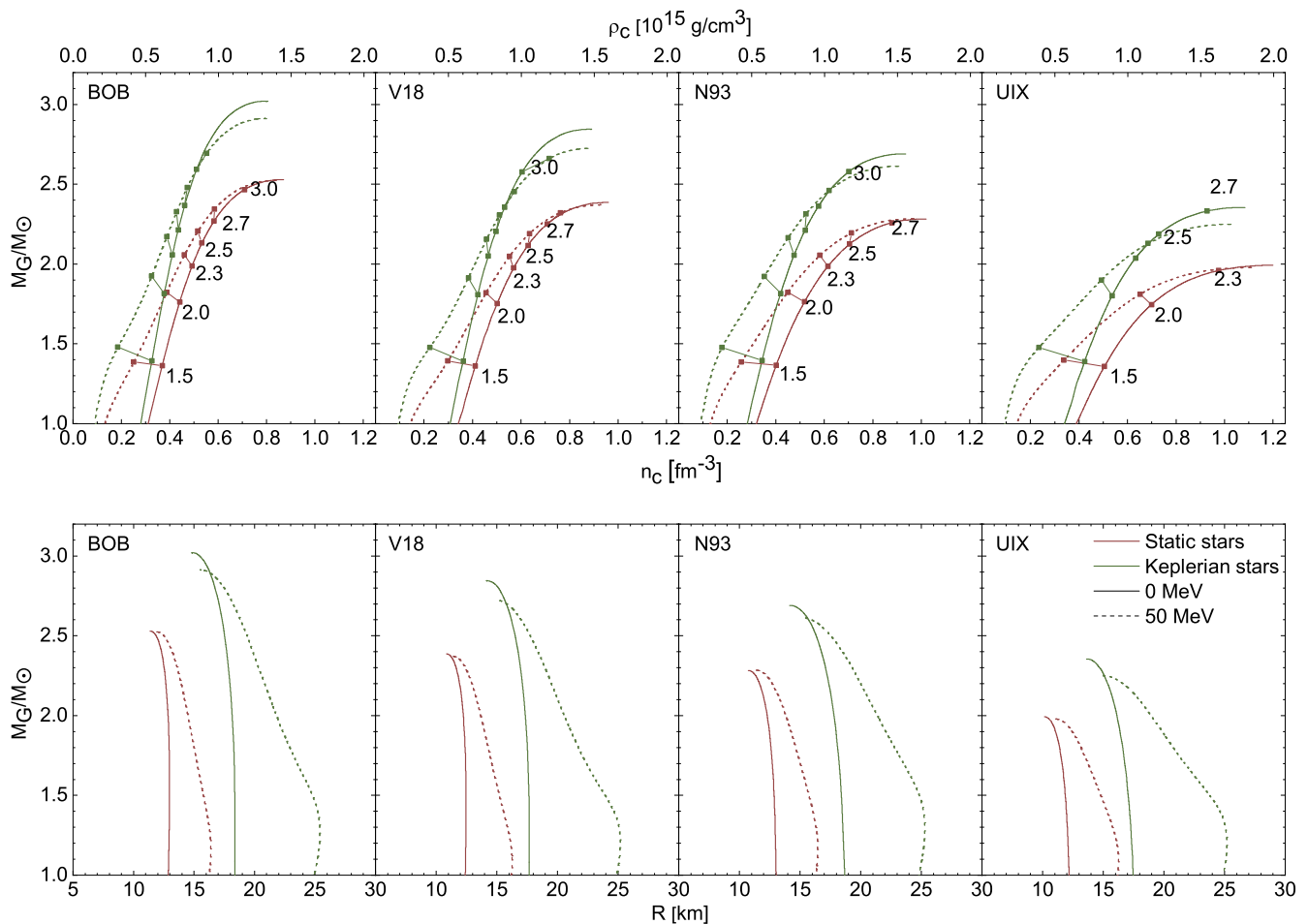


FIG. 1. Gravitational mass vs central density (top row) and radius (bottom row) for static (red curves) and uniformly rotating at f_{Kepler} (green curves) stars at $T = 0$ (solid curves) and $T = 50$ MeV (dashed curves). Configurations of constant baryonic masses M_B/M_\odot (numbers) are indicated by markers and connected by thin lines.

J0030+0451 recently observed by NICER, $M = 1.44^{+0.15}_{-0.14} M_\odot$ and $R = 13.02^{+1.24}_{-1.06}$ km [74], or $M = 1.36^{+0.15}_{-0.16} M_\odot$ and $R = 12.71^{+1.14}_{-1.19}$ km [75].

As seen in Fig. 1 and reported in [44], the dependence of the maximum gravitational mass of static NSs on temperature is very weak, due to a strong compensation between nucleonic and leptonic contributions to the thermal pressure of metastable matter in the BHF approach. However, finite temperature decreases notably the stability (Kepler frequencies and maximum masses) of fast-rotating stars for all EOSs. This is important for the analysis of BNSMs, as essential features of the merger remnant are high temperature (> 50 MeV) and very fast rotation (> 1 kHz), as will be illustrated later. In fact, a merger remnant is expected to be rotating differentially with even higher frequencies than f_{Kepler} , and this allows a metastable transient state before collapse to a black hole with still higher threshold mass M_{th} than the one of rigid rotation, according to the approximate universal relations found in [76, 77], where the threshold mass is related to the maximum mass of the static model M_{TOV} and one other static NS

parameter,

$$M_{\text{th}} = \left(3.06 - \frac{1.01}{1 - 1.34 M_{\text{TOV}}/R_{\text{TOV}}} \right) M_{\text{TOV}}, \quad (9)$$

$$M_{\text{th}} = 0.59 M_{\text{TOV}} + 1.36 M_\odot + 0.80 M_\odot \Lambda_{1.4}/1000, \quad (10)$$

$$M_{\text{th}} = 0.55 M_{\text{TOV}} - 0.20 M_\odot + 0.17 M_\odot R_{1.6}/\text{km}. \quad (11)$$

These estimates are also listed in Table I and might be up to about 20% larger than the ones for rigid rotation for the softest UIX EOS. However, the predictions themselves vary by several percent, the latter values, Eq. (11), being significantly higher for most EOSs.

Thus finite temperature and rotation have opposite effects on the stellar stability and their competition determines the stability limit of a BNSM event, for example. That is why an accurate theoretical determination of the finite-temperature EOS is essential for the analysis of a merger event. No firm conclusions regarding properties of cold NSs can be drawn based on an analysis of a hot merger remnant unless this feature is well under theoretical control.

For the specific case of the GW170817 event, an important

TABLE I. Properties of the maximum mass configurations of static (first row for each EOS) and maximally rotating stars with Kepler frequency (second row) at temperatures $T = 0$ and 50 MeV (values in brackets): gravitational and baryonic masses M and M_B , radius R , and central density n_c . Also listed for comparison and later use are the estimated threshold gravitational mass M_{th} according to Eqs. (9,10,11), the baryonic mass of the merger simulations, Eq. (13), the baryonic mass of the GW170817 object, Eq. (12), the tidal deformability of the individual NSs, and the radius of a cold static NS with mass $1.6M_\odot$.

EOS	f [kHz]	M/M_\odot	M_{th}/M_\odot	M_B/M_\odot	M_B^{sim}/M_\odot	$M_B^{\text{GW170817}}/M_\odot$	R [km]	n_c [fm $^{-3}$]	$\Lambda_{1.35}$	$R_{1.6}$ [km]
BOB	0	2.53 (2.52)	3.17, 3.33, 3.39	3.10 (2.99)	2.95	3.00	11.38 (11.93)	0.87 (0.84)	755	12.98
	1.70 (1.55)	3.02 (2.91)		3.61 (3.33)			14.86 (15.56)	0.80 (0.79)		
V18	0	2.39 (2.37)	3.03, 3.15, 3.23	2.91 (2.79)	2.97	3.01	10.86 (11.40)	0.96 (0.93)	597	12.45
	1.77 (1.61)	2.85 (2.73)		3.38 (3.10)			14.20 (14.86)	0.88 (0.89)		
N93	0	2.28 (2.28)	2.99, 3.14, 3.23	2.73 (2.64)	2.94	3.00	10.72 (11.38)	1.02 (0.97)	701	12.80
	1.73 (1.54)	2.69 (2.61)		3.15 (2.94)			14.15 (15.15)	0.93 (0.90)		
UIX	0	1.99 (1.98)	2.80, 2.80, 2.89	2.35 (2.24)	2.95	3.02	10.16 (11.08)	1.20 (1.11)	434	11.76
	1.72 (1.46)	2.36 (2.25)		2.73 (2.49)			13.61 (15.01)	1.08 (1.03)		

quantity is its total baryonic mass

$$M_B^{\text{GW170817}} \equiv 2M_B(M_G = 1.365M_\odot), \quad (12)$$

which we also list in the table together with the relevant value for the simulations we actually carried out,

$$M_B^{\text{sim}} \equiv 2M_B(M_G = 1.35M_\odot). \quad (13)$$

It depends only very weakly on the EOS. Comparing the values of M_B , M_B^{sim} , and M_B^{GW170817} , we can already draw some important qualitative conclusions: While the BOB, V18, and (marginally) N93 EOSs would be able to sustain even a rigidly rotating hot remnant, the soft UIX EOS would permit only a metastable differentially rotating one. Eventually, the cooling-down remnant would gain stability (not enough for UIX though), but in the long-term spindown, only the BOB EOS would be able to sustain a stable cold and static NS with a mass of M_B^{sim} or M_B^{GW170817} (All this assuming that no mass is ejected). These are very simplistic considerations that we will confront now with our results of the merger simulations.

III. GRAVITATIONAL-WAVE SIGNAL

As a standard approach in numerical relativity, we adopt the Newman-Penrose formalism [78] in order to extract the GW strains for our models. In particular, the Einstein toolkit module WEYLSCAL4 is used in order to calculate the Newman-Penrose scalar ψ_4 at different surfaces of constant coordinate radius r . ψ_4 is then related to the second time derivatives of the GW polarization amplitudes h_+ and h_\times via

$$\psi_4 = \ddot{h}_+ - i\ddot{h}_\times = \sum_{l=2}^{\infty} \sum_{m=-l}^l \psi_4^{\ell m}(t, r) {}_{-2}Y_{\ell m}(\theta, \phi), \quad (14)$$

where we adopt the double-dot notation in order to express the second time derivative and we have also considered the multipole decomposition of ψ_4 in spherical harmonics [79] of spin weight $s = -2$; in our numerical setup, such decomposition is

carried out by the module MULTIPOLE. We restrict our analysis to the $\ell = m = 2$ mode, which represents the dominant one after the merger; in particular, we assume

$$h_{+, \times} = \sum_{l=2}^{\infty} \sum_{m=-l}^l h_{+, \times}^{\ell m}(t, r) {}_{-2}Y_{\ell m}(\theta, \phi) \approx h_{+, \times}^{22}(t, r) {}_{-2}Y_{22}(\theta, \phi). \quad (15)$$

The double integration in time of ψ_4 is performed according to the fixed-frequency integration method described in [80]. Our waveforms are then aligned to the ‘‘time of the merger’’ (as done, e.g., in Ref. [13]), which we impose as $t = 0$ and define as the time when the GW amplitude

$$|h| \equiv \sqrt{h_+^2 + h_\times^2} \quad (16)$$

reaches its global maximum. In our analysis, we also compute the instantaneous frequency of the GWs, defined as in [81],

$$f_{\text{GW}} \equiv \frac{1}{2\pi} \frac{d\chi}{dt}, \quad (17)$$

where $\chi = \arctan(h_\times/h_+)$ represents the phase of the complex waveform. As done in Ref. [13], we identify

$$f_{\text{max}} \equiv f_{\text{GW}}(t = 0) \quad (18)$$

as the instantaneous frequency at amplitude maximum.

An important quantity in our analysis is the power spectral density (PSD) of the effective amplitude,

$$\tilde{h}(f) \equiv \sqrt{\frac{|\tilde{h}_+(f)|^2 + |\tilde{h}_\times(f)|^2}{2}}, \quad (19)$$

where $\tilde{h}_{+, \times}(f)$ represent the Fourier transforms of $h_{+, \times}$, respectively,

$$\tilde{h}_{+, \times}(f) \equiv \int dt e^{-i2\pi ft} h_{+, \times}(t) \quad (20)$$

for $f \geq 0$, and $\tilde{h}_{+, \times}(f) \equiv 0$ for $f < 0$. Our PSDs are first filtered by applying a symmetric time-domain Tukey filter with

parameter $\alpha = 0.25$ to the waveforms, in order to compute PSDs without the artificial noise due to the truncation of the waveforms themselves. We then focus on determining the f_2 peak of the PSD; in this regard, we first fit our data with the analytic function [82]

$$S_2(f) = A_{2G} e^{-(f-F_{2G})^2/W_{2G}^2} + A(f)\gamma(f), \quad (21)$$

where

$$A(f) \equiv \frac{1}{2W_2} [(A_{2b} - A_{2a})(f - F_2) + W_2(A_{2b} + A_{2a})], \quad (22)$$

$$\gamma(f) \equiv \left(1 + e^{-(f-F_2+W_2)/s}\right)^{-1} \left(1 + e^{(f-F_2-W_2)/s}\right)^{-1}. \quad (23)$$

The peak frequency is then determined by

$$f_2 \equiv \frac{\int df S_2(f) f}{\int df S_2(f)}. \quad (24)$$

An intrinsic uncertainty, due to both the choice of the fitting functions and parameters, and the integration interval, affects the fitting procedure, and we estimate the latter as ± 10 Hz; this estimate is later added in quadrature to a systematic deviation of the value we find for f_2 from the nearest (local) maximum of the PSD curve, which in all our cases also coincides with the global maximum.

We complete our analysis with the calculation of the total emitted energy for the $\ell = m = 2$ mode, namely

$$E_{\text{GW}} = \frac{R^2}{16\pi} \int dt \int d\Omega |\dot{h}(t, \theta, \phi)|^2, \quad (25)$$

where Ω labels the solid angle and R represents the source-detector distance.

IV. MERGER SIMULATIONS

Before illustrating the results of the merger simulations, we briefly review the mathematical and numerical setup that we adopt. This is similar to the one of Ref. [11] and discussed in great detail in Ref. [83], to which we refer the interested reader for additional information.

Our models employ initial data for irrotational binary NSs computed using the multi-domain spectral-method code LORENE [84, 85]. In our case all initial data, modeled considering a zero-temperature, beta-equilibrated cut of the full EOS tables, involve equal-masses binaries with a gravitational mass $M_G = 1.35 M_\odot$ at infinite separation (corresponding to a total baryonic mass $M_B^{\text{sim}} \approx 2.94 - 2.97 M_\odot$ slightly dependent on the EOS, given in Table I), and an initial separation between the stellar centers of 45 km. We stress that with this choice our simulations can reproduce closely the GW170817 merger event, in which the detected chirp mass $M_{\text{chirp}} = 1.188 M_\odot$ corresponds to $M_G = 1.365 M_\odot$ for a symmetric binary system [1].

We perform our simulations in full general relativity using for the spacetime evolution the fourth-order finite-differencing McLachlan code [86], part of the publicly available Einstein toolkit [87], with the inclusion of a fifth-order

Kreiss-Oliger-type artificial dissipation [88] to ensure the non-linear stability of the evolution. In particular, our simulations adopt the CCZ4 formulation of the Einstein equations [89–91], where the evolution of the gauge variables is carried out by using a “1+log” slicing condition for the lapse function and a “Gamma driver” condition for the shift vector (see, e.g., Refs. [92, 93]). In our setup, the WhiskyTHC code [72, 94, 95] is used in order to solve the general-relativistic hydrodynamics equations; in particular, the latter employs either finite-volume or high-order finite-differencing high-resolution shock-capturing methods and, for our simulations, we adopt the HLLC Riemann solver and the high-order MP5 primitive reconstruction [96, 97]. The coupled set of the space-time and hydrodynamic equations is integrated in time using the method of lines with an explicit third-order Runge-Kutta method, where a Courant-Friedrichs-Lewy (CFL) parameter of 0.15 is used in order to compute the timestep. Regarding our grid setup, we employ the Carpet driver [98], which operates, with an adaptive-mesh-refinement approach, the following grid hierarchy: we consider six refinement levels with a grid resolution which ranges from $\Delta h_5 = 0.16 M_\odot$ (i.e., ~ 236 m) for the finest level to $\Delta h_0 = 5.12 M_\odot$ (i.e., ~ 7.5 km) for the coarsest level, whose outer boundary is placed at $1024 M_\odot$ (i.e., ~ 1515 km). Our setup also makes use of a reflection symmetry across the $z = 0$ plane in order to reduce the computational resources needed.

Neutrino emission acts as cooling mechanism and is implemented in our temperature-dependent simulations. We treat the effects on matter due to weak reactions using the gray (energy-averaged) neutrino-leakage scheme described in Refs. [99, 100], and evolve free-streaming neutrinos according to the M0 heating scheme introduced in Refs. [37, 100]. This is accompanied by a loss of betastability of the heated stellar matter that was analyzed in detail in Ref. [11].

Our simulations do not include a treatment for viscous effects, although it has been shown (see Refs. [35, 37, 41, 101, 102] for a complete discussion) that the latter have an impact on several features of the remnant, such as the angular velocity distribution, the emitted GW signal, and ejecta properties. As a consequence, and as better investigated in the next chapter, we do not expect a significant slowdown of rotation in the timespan we consider in our simulations.

Our EOS tables cover a range $5.1 \leq \log_{10}(\rho / \text{g/cm}^3) \leq 16$ in rest-mass densities, with a spacing $\Delta \log_{10}(\rho / \text{g/cm}^3) = 0.1$, for a total of 110 points; temperature ranges from $-1.0 \leq \log_{10}(T/\text{K}) \leq 2.6$, with a spacing $\Delta \log_{10}(T/\text{K}) = 0.04$ for a total of 91 points, and electron fractions cover the range $0.01 \leq Y_e \leq 0.65$, where the spacing is $\Delta Y_e = 0.01$, for a total of 65 points. Our tables are first prepared in the same format as the one discussed in Appendix A of Ref. [19]; we then use the routines present in [103] in order to create versions of the EOSs compatible with WhiskyTHC. The latter code contains routines in order to carry out either linear or cubic spline interpolations on the original tables; the code is also responsible for the time evolution of proton and neutron number densities, guaranteeing the local conservation of both species (see Ref. [100] for a detailed description).

We stress that, while the V18 EOS has already been studied

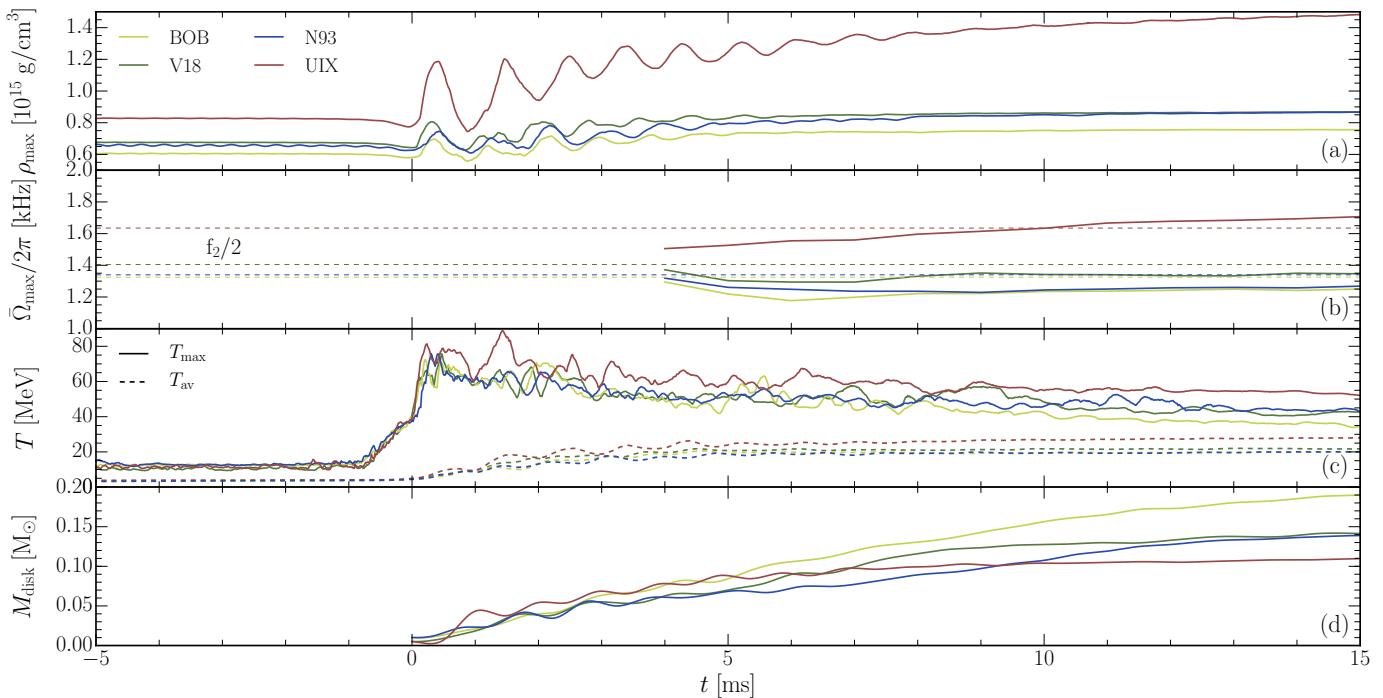


FIG. 2. Maximum values of rest-mass density (a) and azimuthally-averaged differential rotational frequency (b), maximum T_{\max} and average T_{av} temperature (c), and disk mass (d) as a function of time for the simulations using the four different EOSs.

in Ref. [11], the BOB, N93, and UIX EOSs are employed here for the first time in merger simulations. In the following we present the results.

V. RESULTS AND DISCUSSION

All the simulations presented here follow the remnant evolution for a period of at least 15 ms. We set our time coordinate such that $t = t_{\text{merg}} = 0$, where t_{merg} is the time of the merger and corresponds to the maximum of the GW amplitude. We notice that for all EOSs the merger simulations produce a metastable hypermassive NS during this time, when the remnant is still stabilized by differential rotation and finite temperature. This feature is compatible with the multimessenger analysis of the GW170817 event [104].

A. Stellar matter

As a first illustration of the typical properties of the stellar matter in the postmerger phase, Fig. 2 shows for the different cases we have studied the evolution of the maximum rest-mass density ρ_{\max} (a), the maximum azimuthally-averaged differential rotation frequency $\bar{\Omega}_{\max}/2\pi$ (b), the maximum and averaged temperatures T_{\max} and T_{av} (c), the latter quantities evaluated in the $z = 0$ plane, and the mass of the disk (d). We now discuss the results in detail.

We find that the simulations performed with the most realistic V18 and N93 EOSs lead to a remnant with ρ_{\max} of about $0.9 \times 10^{15} \text{ g/cm}^3$, and also similar values of the maximum and

average temperatures. These two EOSs feature also similar common properties for the static and Kepler configurations, see Table I. Consistently, the post-merger remnant modeled with the BOB EOS, which is the stiffest EOS in our sample, reaches the smallest maximum density and temperature, whereas the (too) soft UIX case exhibits the typical increasing central density signature of a model experiencing a collapse after the merger (although not within our simulation timespan), which would be in agreement with the characteristics of this EOS discussed in Sec. II B. Namely, we notice that the maximum mass of the UIX Keplerian configurations, reported in Table I, is well below the mass of the remnant, and therefore it might be only temporarily supported by differential rotation. The subsequent collapse would require first a slowdown of the stabilizing differential rotation, which should occur on a typical time scale of milliseconds for a too soft EOS like UIX [5, 11, 33, 105], although in our simulation we did not detect it within 20 ms.

The determination of the actual, much longer, collapse time of the GW170817 remnant is a very delicate task, since it depends on several physical processes, e.g., the time evolution of the differential rotation [33, 106], ejection of matter [100, 107, 108], and viscosity effects [38, 109, 110]. A tentative approach has been recently discussed in Ref. [104], where the properties of the kilonova emission [2] have been combined with the delay time between the GW chirp signal and the prompt gamma-ray emission onset in GRB 170817A [111], in order to estimate a collapse time of the HMNS of about 1 second. Realistic EOSs like V18 or N93, combined with an elaborate simulation procedure taking into account with sufficient accuracy all the above (micro)physics ingredients, would be

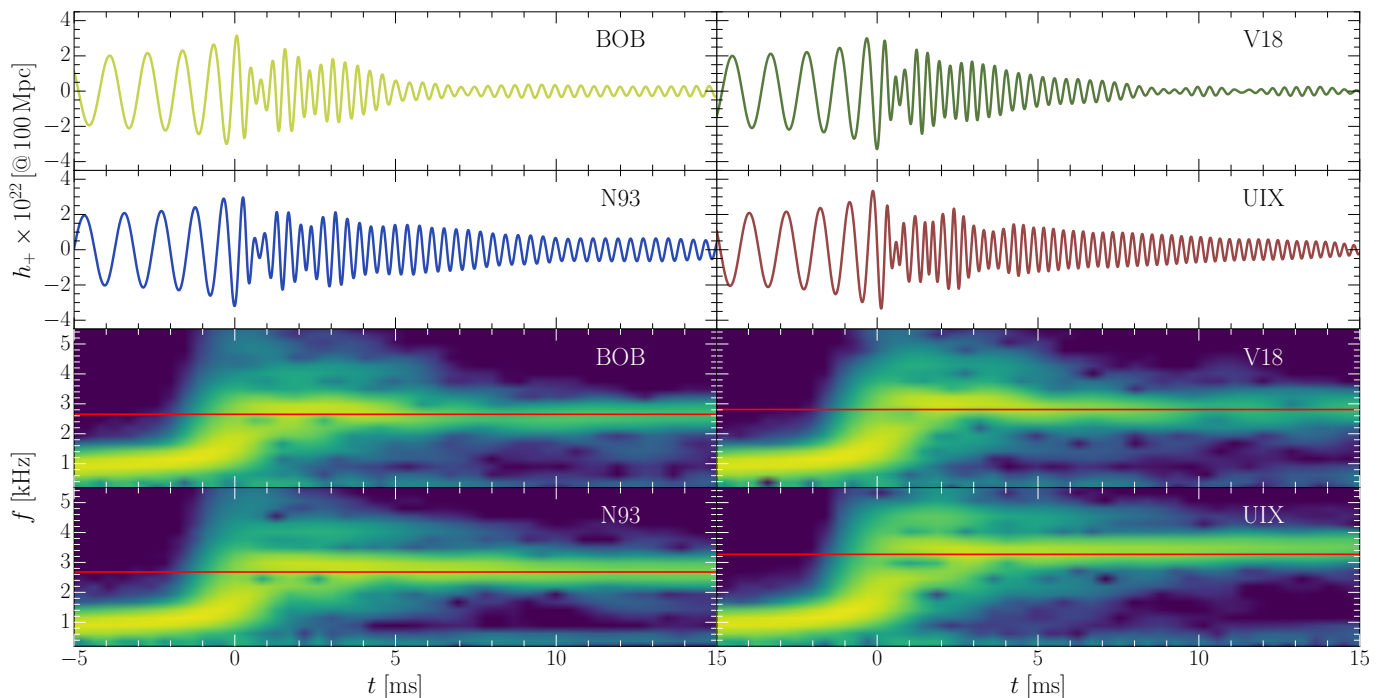


FIG. 3. Upper panels: gravitational waveforms over a time scale of 15 ms after the merger for the four simulated models obtained for gravitational masses $2 \times 1.35 M_{\odot}$. Lower panels: the spectrograms for all the considered cases; red lines represent the position of the f_2 peaks (Table II).

expected to predict compatible values. At the current stage we are still far from this situation.

We nevertheless continue our analysis of the numerical results regarding rotational properties of the remnant. Panel (b) of Fig. 2 shows the time development of the maximum of the azimuthally-averaged differential rotation frequency [33] on the equatorial plane (see Fig. 5),

$$\bar{\Omega}(r, t) \equiv \frac{1}{4\pi\Delta t} \int_{t-\Delta t}^{t+\Delta t} dt' \int_{-\pi}^{\pi} d\phi \Omega(z=0, r, \phi, t') \quad (26)$$

with $\Delta t = 0.5$ ms. Values are sampled at each ms starting from 4 ms after the merger, as for earlier times the system is still too asymmetric.

Again the BOB, V18, and N93 EOS exhibit common features, whereas UIX displays a different trend. While the profile for the UIX EOS shows an increasing unstable behavior in the time window analyzed here, which is compatible with the increase of ρ_{\max} discussed before, the other EOSs show stable profiles, thus indicating no slowdown of rotation within the milliseconds time interval simulated here. Therefore an eventual collapse with these EOSs, related to loss of stabilizing rotation, could occur only much later.

For completeness (c.f., [33]), dashed horizontal lines shown in the same panel represent for each EOS the quadrupole peak frequency $f_2/2$, Eq. (24), determined via the PSDs shown in the next section. We see that the maximum differential rotation frequencies are systematically slightly lower than the f_2 -related frequencies. This is not surprising, since the latter values are determined through PSDs considering also the first 4 ms, when the remnant is rotating slightly faster.

In panel (c) of Fig. 2 we plot both the maximum temperature (solid curves) and the density-weighted average temperature (dashed curves), defined as

$$T_{\text{av}} \equiv \frac{\int dV \rho T}{\int dV \rho}. \quad (27)$$

All the simulations feature maximum temperatures which remain in general lower than 70 MeV in the post-merger phase. As already shown in Ref. [11], however, maximum temperatures are reached only in local hot spots, and are not representative of the average temperature of matter, which is about 20 to 30 MeV. Typical temperatures depend slightly on the EOS, with softer (stiffer) ones producing higher (lower) temperatures.

We also monitor the disk mass M_{disk} (discussed in Sec. V C) as function of time, shown in Fig. 2(d). We notice that during the short timespan of the simulations, the disk masses are still increasing, but tend to become stable at the end of our time evolution, where they span a range comprised between 0.1 and $0.2 M_{\odot}$, as also reported in Table II. The softest UIX EOS attracts most material into the dense core and produces the lightest disk, contrary to the stiffest BOB model, which is instead responsible of a large $M_{\text{disk}} \approx 0.2 M_{\odot}$.

B. Gravitational-wave signal

We now turn to the analysis of the GW signal. In Fig. 3 (upper panels) we show the plus polarization of the $l = m = 2$ component of the GW strains, which we label as h_+ , Eq. (15),

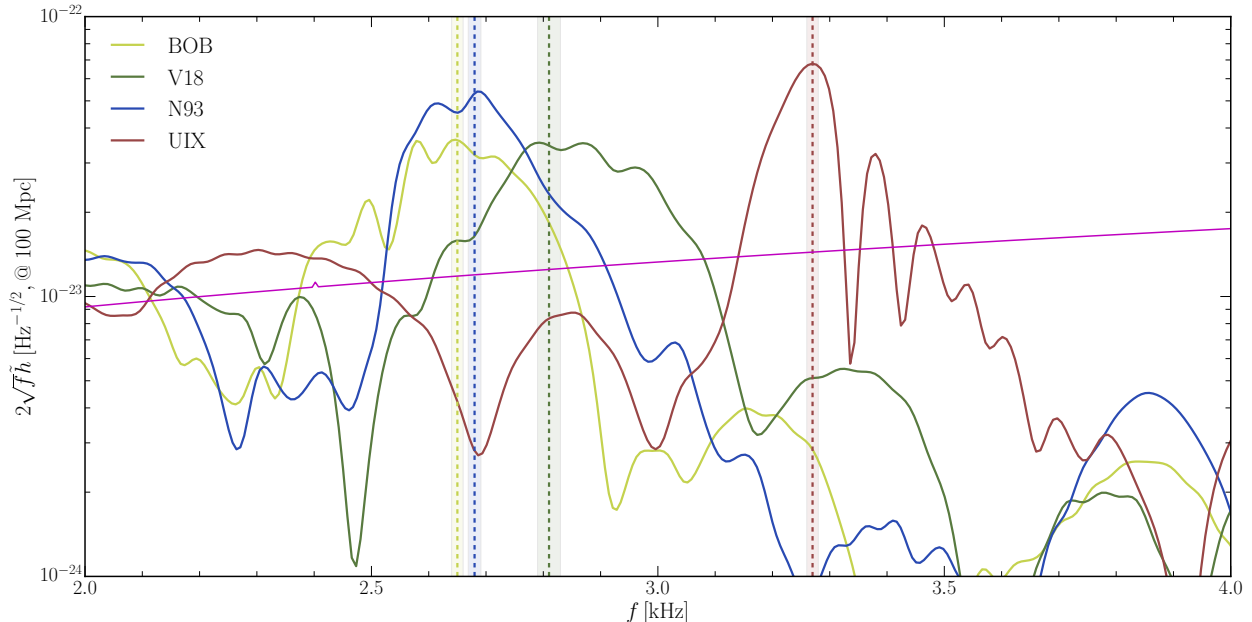


FIG. 4. PSDs \tilde{h} , Eq. (19), of the simulations evaluated at a distance of 100 Mpc. Vertical dashed lines of different colors indicate the frequency of the main postmerger peak f_2 and estimated error. The sensitivity curve (magenta color) of Advanced LIGO is displayed for reference.

TABLE II. Properties of the simulated models: frequency of the f_2 peak, frequency at maximum amplitude f_{\max} , the total emitted GW energy until $t = 15$ ms E_{GW} , and baryonic masses of the object M_{obj} , the disk M_{disk} , the ejected matter M_{ej} at $t = 15$ ms. The f_2 values in brackets are obtained using the universal relations Eqs. (28,29,30). The M_{disk} values in brackets are obtained using the universal relation Eq. (25) of [37].

EOS	f_2 [kHz]	f_{\max} [kHz]	E_{GW} [10^{52} erg]	M_{obj} [M_{\odot}]	M_{disk} [M_{\odot}]	M_{ej} [$10^{-3} M_{\odot}$]
BOB	2.65 ± 0.01 (2.62, 2.65, 2.82)	1.68	4.10	2.76	0.189 (0.139)	3.7
V18	2.81 ± 0.02 (2.90, 2.86, 2.96)	1.77	4.88	2.82	0.141 (0.093)	4.2
N93	2.68 ± 0.01 (2.67, 2.72, 2.87)	1.68	5.99	2.81	0.138 (0.124)	4.5
UIX	3.27 ± 0.01 (3.23, 3.19, 3.14)	1.91	7.69	2.85	0.109 (0.044)	7.4

for all the considered simulations we have carried out using different microscopic EOSs. All models feature an instant of the merger of about 15 ms from the start of the simulation, identified as previously mentioned as the time corresponding to the maximum strain amplitude. One can roughly observe that the oscillations for the more stable EOSs with higher M_{\max} (BOB and V18) are ‘ringing down’ faster than for the others, which is the expected behavior [13, 82].

The evolution of the characteristic frequencies for the cases we have considered is also evidenced in the lower panels of the figure, where the spectrograms of the four models are shown. In order to compute them, we calculate the spectra by first segmenting the h_+ signals in pieces of ≈ 5 ms each; a Blackman window is then applied to the segments, which are overlapped by 90%, similarly to what is done in Ref. [13]. As clearly visible, while shortly after the merger different significant frequencies are present, like the f_1 or the f_3 peaks (whose investigation is not reported here), the $l = m = 2$ frequency (denoted in the plots with a red dashed line for each case) and its related f_2 peak (following the same nomenclature as in Ref. [13]) is the only robust feature which is present from the time of the merger to the end of the considered time window for all our models.

Fig. 4 shows the power spectral density (PSD) plots of all simulations, determined as detailed in Sec. III. In particular, we choose to study the dominant $l = m = 2$ mode, and consider the position of the f_2 peak as a tracker of the different behaviors. Since, except for the UIX case, it is difficult to distinguish the dominant f_2 peaks by eye, the fitting procedure discussed in Sec. III represents the only way for an accurate determination of the f_2 positions, which are shown in the figure together with the estimated errors.

We also report in Table II these values, together with other relevant GW properties for each simulation; in particular, we determine for each case the maximum frequency f_{\max} , Eq. (18), and the emitted GW energy E_{GW} for the $l = m = 2$ mode, Eq. (25), both measured as outlined in Sec. III. We find that the UIX EOS predicts by far the highest frequency for the f_2 peak, more than 400 Hz higher than the other cases; this represents a spectroscopical confirmation of this remnant being the most dense (see the maximum rest-mass density shown in Fig. 2) and the fastest rotating of all the cases we considered, since the frequency of the mode scales with the square root of the average density (see, e.g., Ref. [112]).

For comparison we also list (in brackets) the values of f_2 according to universal relations between f_2 and the radius $R_{1,6}$ of

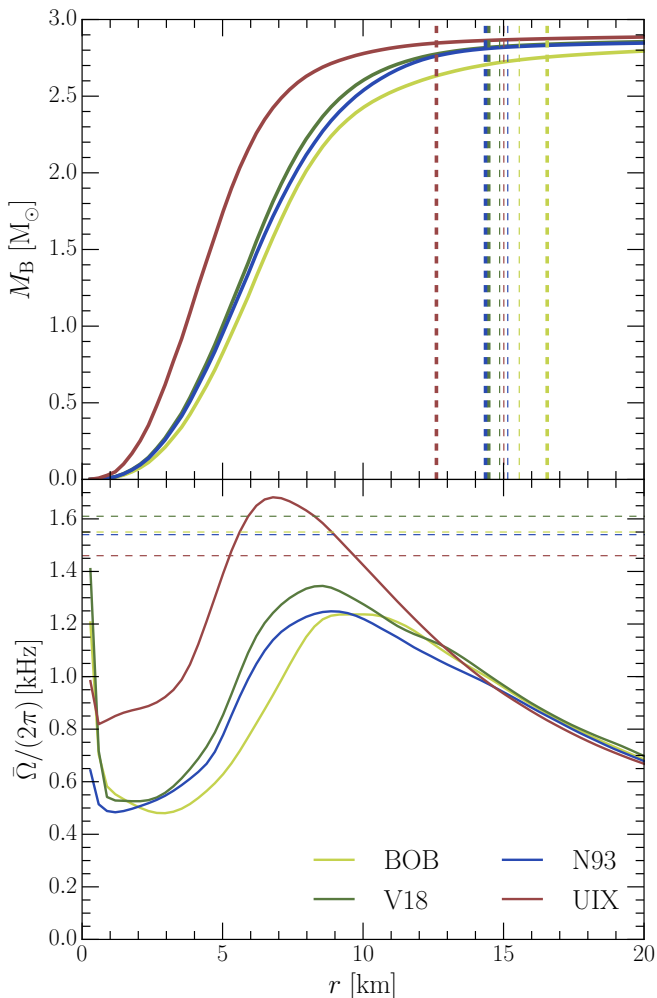


FIG. 5. Upper panel: Enclosed baryonic mass M_B as a function of spherical radius r at $t = 15$ ms for the different EOSs. Thick dashed lines denote radii corresponding to M_{obj} in Table II. Thin dashed lines are the radii of $T = 50$ MeV M_{max} Kepler configurations in Table I. Lower panel: Azimuthally-averaged angular velocity, Eq. (26), as a function of the radial cylindrical coordinate r (at $z = 0$) at $t = 15$ ms. Thin horizontal dashed lines indicate the Kepler frequencies of the $T = 50$ MeV M_{max} configurations for the different EOSs listed in Table I.

a $1.6M_{\odot}$ NS [113], the chirp mass M_{chirp} [114], and the tidal deformability parameter Λ [13] proposed in different publications,

$$f_2[\text{kHz}] \approx \begin{cases} 6.284 - 0.2823 R_{1.6} & (f_2 < 2.8 \text{ kHz}) \\ 8.713 - 0.4667 R_{1.6} & (f_2 > 2.8 \text{ kHz}) \end{cases}, \quad (28)$$

$$f_2[\text{kHz}] \approx 13.82M_c - 0.576M_c^2 + 0.479M_c^3 - 1.375R_{1.6}M_c - 0.073R_{1.6}M_c^2 + 0.044R_{1.6}^2M_c, \quad (29)$$

$$f_2[\text{kHz}] \approx 5.832 - 0.8\Lambda^{1/5}, \quad (30)$$

where $M_c \equiv M_{\text{chirp}}/M_{\odot}$ and $R_{1.6}$ is given in km. Both $R_{1.6}$ and Λ are listed in Table I. One observes a reasonable agreement (within 3%) in particular for the first correlation with the

radius, whereas the last one with Λ is less pronounced with about 7% possible deviations, as in [13].

Interestingly, as shown, e.g., in Refs. [11, 115], the position of the theoretical f_2 peak may change up to several tens Hz when simulations are performed with the same zero-temperature EOS and initial data, but employing the approximate hybrid finite-temperature EOS approach with different values of the thermal index Γ_{th} . We refer the interested reader to the latter references for complete discussions.

C. Masses and ejecta

We also list in Table II, for the instant $t = 15$ ms, the baryonic masses of the remnant M_{obj} and its disk M_{disk} , obtained by integrating the conserved rest-mass density over the respective 3D domains (We choose 10^{13} g/cm³ as the boundary density between object and disk, which represents a common choice in literature, see, e.g., Ref. [116]),

$$M_B = \int d^3r D, \quad D = \sqrt{\gamma} W \rho, \quad (31)$$

where γ represents the 3-metric determinant and W is the Lorentz factor. From Fig. 2 it seems that at $t = 15$ ms nearly stable values have been reached [105], apart for the UIX EOS.

We remind that lower limits on the disk mass of GW170817 derived from its electromagnetic counterpart are about $M_{\text{disk}} \gtrsim 0.04M_{\odot}$ [37, 40, 117], with which all our EOSs would comply. An approximate universal relation between M_{disk} and Λ has been proposed in Ref. [37] and we list those values also in Table II. However, it can be seen that the deviations are very large, which has also been pointed out in [40].

To measure the properties (baryonic mass M_{ej}) of the dynamical ejecta (treated as perfect fluid; no nuclear reaction network is present in the code), we consider multiple spherical detectors at different radii around the origin, taking the detector at $200M_{\odot} \approx 300$ km for our measurements. In order to determine which of the material crossing this surface is effectively unbound, we set a threshold according to the geodesic criterion, as done, for example, in Refs. [83, 105]. In detail, a particle on geodesics is considered to be unbound if the covariant time component of the fluid four-velocity u satisfies $u_t \leq -1$ (see, e.g., Ref. [108] for a discussion of the method).

In the following we analyze in more detail properties of the remnant that is formed after the merger. Fig. 5 (upper panel) shows the profiles of the enclosed baryonic mass M_B as a function of the spherical radius r at $t = 15$ ms after the merger; we perform such calculation for all the cases we have investigated by computing volume integrals of the conserved rest-mass density D up to each different spherical radius r . The results show that the softest of our EOS sample, UIX, leads to the most compact remnant and viceversa for the BOB EOS, which is the stiffest EOS. For every case, a thick dashed vertical line denotes the M_{obj} position, according to Table II (although due to the density-cutoff procedure M_{obj} is not the mass of a spherical object). Again, the V18 and N93 EOSs lead to very similar profiles, as also for other global properties in Table I. Thin dashed vertical lines indicate the radii of the

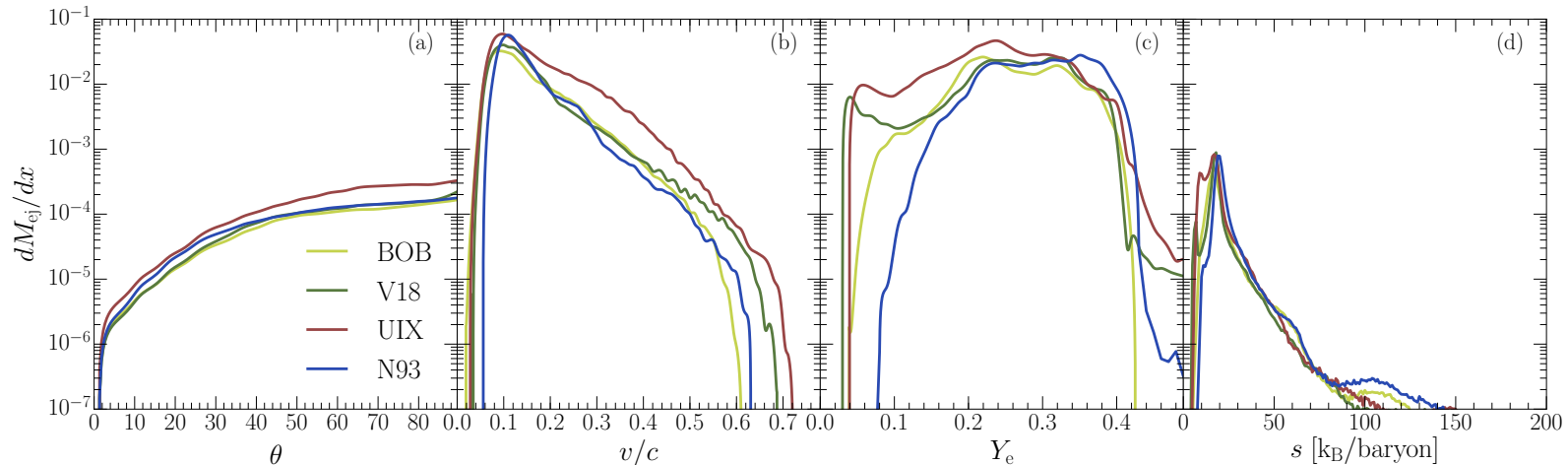


FIG. 6. Distribution of the ejected mass as functions of the polar angle θ (a), velocity ratio v/c (b), electron fraction Y_e (c), and specific entropy s (d). Curves are normalized with respect to the total ejected mass values M_{ej} enlisted in Tab. II.

$T = 50$ MeV Kepler configurations (Table I) for a qualitative comparison. In fact we note for BOB, V18, N93 quite similar values and trends as the remnant radii, whereas the UIX remnant radius at $t = 15$ ms is significantly smaller than the one of stable Kepler rotation, which points again to the commencing collapse of this object.

In Fig. 5 (lower panel) we illustrate the angular velocity profiles for the four remnants at $t = 15$ ms. In particular, we perform averages in the azimuthal direction on the equatorial plane ($z = 0$) and over a time window of 1 ms at $t = 15$ ms, see Eq. (26), so as to obtain functions that depend only on the cylindrical radius r from the center of the grid. The EOSs considered here exhibit a maximum of the averaged angular velocity located at approximately $r \approx 8$ km, roughly corresponding to the position where the two hot spots appeared at the beginning of the merger [33]. Unsurprisingly, the maximum reached value is highest for the UIX EOS, a feature which is fully compatible with our findings in the PSD distribution, and also seen in Fig. 2(d). Also in this panel the horizontal dashed lines denote the Kepler frequencies of the $T = 50$ MeV M_{max} configurations for a qualitative comparison. Once again the unstable nature of the UIX simulation is confirmed by local rotation substantially above Kepler frequency. We also point out that the profiles we have determined are in agreement with results related to other EOSs (see, e.g., [33, 41]) and that, according to our results with the V18 EOS in Ref. [11], we expect that such average profiles remain robust even when the same simulation is carried out with the hybrid EOS approach, choosing reasonable values for the Γ_{th} parameter.

Finally, we study in detail the properties of the dynamical ejecta in Fig. 6; in particular, we characterize the mass ejection dependence on the polar angle [panel (a); here, 0° refers to the z axis, while 90° is representative of the equatorial plane], the velocity ratio v/c (b), the electron fraction Y_e (c), and the specific entropy s (d). In particular, the specific entropy (which is directly related to the temperature of the ejected matter), the velocity, and the electron fraction represent the most important quantities in order to characterize

the r-process nucleosynthesis in the outflows [118].

We determine that the emission increases almost monotonically with the polar angle for all our cases, with this behavior being particularly evident up to about 50° , while the curves flatten out after this angle. Thus the tidal disruption of matter generates ejecta which are mostly distributed close to the equatorial plane (labeled as equatorial ejecta in [119]).

Also the velocity distribution shows common features for all the cases we analyze: in particular, a clear peak at $v/c \approx 0.1$ is present, after which the distribution decreases up to values between 0.6 and 0.75. The tails of the distribution are ordered according to the stiffness of the EOS, i.e., softer EOSs (UIX) eject more energetic matter. These features are compatible with the cases analyzed in Ref. [116], where different EOSs were considered.

The electron fraction represents a crucial parameter in order to determine which elements can be created by the r-process; indeed, heavy elements ($A \gtrsim 120$) are created via neutron-rich ejecta ($Y_e \lesssim 0.25$) [119, 120], whereas neutron-poor ejecta produce elements with lower masses. Different Y_e distributions also have an impact on the kilonova signal: neutron-rich ejecta favor the so-called “red” kilonovae, peaking in the infrared, while neutron-poor ejecta produce “blue” kilonovae [121]. Since our sample of simulations comprises only equal-mass mergers, the resulting distributions favor the presence of the shocked component over the tidal one [116]. For our set of EOSs, in particular, the ejecta distributions start at about $Y_e = 0.04$ with UIX and V18 showing a local maximum at that point. A notable exception is the N93, whose distribution is from $Y_e = 0.08$. We note that N93 is the model with the largest nuclear symmetry energy [8, 46] and would thus inhibit more the ejection of neutron-rich matter. For all our cases, the distributions cover a wide range of Y_e , a feature which is however strongly dependent on the neutrino treatment in the simulations, which redistributes the electron number due to weak interactions, see, e.g., Refs. [37, 100] for further details.

The study of the specific entropy, which, as pointed out in Ref. [83], has a close connection with the shock-heated matter in the ejecta, shows that for all our EOSs, a major fraction

of the ejecta is characterized by low temperatures. Interestingly, all our cases show a prominent peak corresponding to $s \sim 20 k_B/\text{baryon}$ followed by a continuous drop. UIX indeed shows a lower satellite peak at about $s \sim 10 k_B/\text{baryon}$, i.e., a higher fraction of matter is expelled at lower temperature for this unstable transient state.

We close by repeating that without good theoretical and numerical control on neutrino radiation and nuclear viscosity no reliable quantitative predictions for (dynamical and secular) ejecta properties can be made currently.

VI. SUMMARY

We have presented the first simulations of a $2 \times 1.35 M_\odot$ NS merger employing four microscopic temperature-dependent EOSs derived in the BHF formalism that fulfil all current empirical constraints by nuclear phenomenology, and also respect recent limits on maximum NS mass and deformability. All simulations have been performed with a consistent treatment of finite-temperature effects, going beyond what is usually done in the hybrid EOS approach. A detailed comparison of both approaches was made in Ref. [11]. We presented in particular a detailed study of the GW and hydrodynamical properties and focused on analyzing the mass distribution of the post-merger remnant and the properties of the ejected matter. We also examined the validity of several universal relations for these EOSs.

We found that two of the EOSs, V18 and N93 (with $M_{\text{max}} \approx$

$2.3\text{--}2.4 M_\odot$), are good candidates for a realistic modeling of the GW170817 event, whereas the UIX is too soft with a low $M_{\text{max}} \approx 2.0 M_\odot$ and related immediate onset of instability of the remnant. The BOB EOS on the other hand is rather stiff ($M_{\text{max}} \approx 2.5 M_\odot$), and the only one that would be able to support even a static object as massive as the GW170817 remnant, which makes it also appear less realistic.

However, in order to draw firm conclusions of this kind, still a lot of progress in the theoretical and numerical modeling of the post-merger phase is required, in particular an accurate quantitative understanding of viscosity, heat transfer, neutrino reactions, magnetic fields, etc., in the relevant superdense matter. This is absolutely essential for a realistic modeling of the temporal evolution of the remnant and the related GW signal. Only then can really quantitative constraints on the EOS be deduced from future observations of the post-merger GW signal.

ACKNOWLEDGMENTS

We acknowledge useful discussions with R. De Pietri, D. Radice, L. Rezzolla, and K. Takami. Partial support comes from ‘‘PHAROS,’’ COST Action CA16214. Simulations have been carried out on the MARCONI cluster at CINECA, Italy. This work is also sponsored by the National Natural Science Foundation of China under Grant Nos. 11475045, 11975077 and the China Scholarship Council, No. 201806100066.

-
- [1] B. P. Abbott, R. Abbott, T. D. Abbott, F. Acernese, K. Ackley, C. Adams, T. Adams, P. Addesso, R. X. Adhikari, V. B. Adya, and et al. (LIGO Scientific Collaboration and Virgo Collaboration), *Phys. Rev. Lett.* **119**, 161101 (2017).
 - [2] The LIGO Scientific Collaboration, the Virgo Collaboration, B. P. Abbott, R. Abbott, T. D. Abbott, F. Acernese, K. Ackley, C. Adams, T. Adams, P. Addesso, R. X. Adhikari, V. B. Adya, and et al. (LIGO Scientific Collaboration and Virgo Collaboration), *Astrophys. J. Lett.* **848**, L12 (2017).
 - [3] B. Margalit and B. D. Metzger, *Astrophys. J. Lett.* **850**, L19 (2017).
 - [4] L. Rezzolla, E. R. Most, and L. R. Weih, *Astrophys. J. Lett.* **852**, L25 (2018).
 - [5] D. Radice, A. Perego, F. Zappa, and S. Bernuzzi, *Astrophys. J. Lett.* **852**, L29 (2018).
 - [6] V. Paschalidis, K. Yagi, D. Alvarez-Castillo, D. B. Blaschke, and A. Sedrakian, *Phys. Rev. D* **97**, 084038 (2018).
 - [7] G. F. Burgio, A. Drago, G. Pagliara, H.-J. Schulze, and J.-B. Wei, *Astrophys. J.* **860**, 139 (2018).
 - [8] J.-B. Wei, A. Figura, G. F. Burgio, H. Chen, and H.-J. Schulze, *Journal of Physics G Nuclear Physics* **46**, 034001 (2019).
 - [9] B. P. Abbott, R. Abbott, T. D. Abbott, F. Acernese, K. Ackley, C. Adams, T. Adams, P. Addesso, R. X. Adhikari, V. B. Adya, and et al. (LIGO Scientific Collaboration and Virgo Collaboration), *Physical Review Letters* **121**, 161101 (2018).
 - [10] A. Perego, S. Bernuzzi, and D. Radice, *Eur. Phys. J. A* **55**, 124 (2019).
 - [11] A. Figura, J.-J. Lu, G. F. Burgio, Z.-H. Li, and H.-J. Schulze, *Phys. Rev. D* **102**, 043006 (2020).
 - [12] A. Bauswein and H.-T. Janka, *Phys. Rev. Lett.* **108**, 011101 (2012).
 - [13] L. Rezzolla and K. Takami, *Phys. Rev. D* **93**, 124051 (2016).
 - [14] A. Bauswein, N.-U. F. Bastian, D. B. Blaschke, K. Chatziioannou, J. A. Clark, T. Fischer, and M. Oertel, *Physical Review Letters* **122**, 061102 (2019).
 - [15] E. R. Most, L. Jens Papenfort, V. Dexheimer, M. Hanauske, H. Stoecker, and L. Rezzolla, *European Physical Journal A* **56**, 59 (2020).
 - [16] L. Baiotti, *Progress in Particle and Nuclear Physics* **109**, 103714 (2019).
 - [17] D. Radice, S. Bernuzzi, and A. Perego, *Annual Review of Nuclear and Particle Science* **70**, 95 (2020).
 - [18] L. Rezzolla, P. Pizzochero, D. I. Jones, N. Rea, and I. Vidaña, *The Physics and Astrophysics of Neutron Stars*, Vol. 457 (2018).
 - [19] H. Shen, H. Toki, K. Oyamatsu, and K. Sumiyoshi, *The Astrophysical Journal Supplement Series* **197**, 20 (2011).
 - [20] S. Typel, G. Röpke, T. Klähn, D. Blaschke, and H. H. Wolter, *Phys. Rev. C* **81**, 015803 (2010).
 - [21] M. Hempel, T. Fischer, J. Schaffner-Bielich, and M. Liebendörfer, *Astrophys. J.* **748**, 70 (2012).
 - [22] A. W. Steiner, M. Hempel, and T. Fischer, *Astrophys. J.* **774**, 17 (2013).
 - [23] S. Banik, M. Hempel, and D. Bandyopadhyay, *Astrophys. J. Suppl.* **214**, 22 (2014).

- [24] J. M. Lattimer and F. D. Swesty, *Nucl. Phys. A* **535**, 331 (1991).
- [25] H. Togashi, E. Hiyama, Y. Yamamoto, and M. Takano, *Phys. Rev. C* **93**, 035808 (2016).
- [26] H.-T. Janka, T. Zwerger, and R. Mönchmeyer, *Astron. Astrophys.* **268**, 360 (1993).
- [27] A. Bauswein, H. Janka, and R. Oechslin, *Phys. Rev. D* **82**, 084043 (2010).
- [28] L. Baiotti, B. Giacomazzo, and L. Rezzolla, *Phys. Rev. D* **78**, 084033 (2008).
- [29] K. Hotokezaka, K. Kyutoku, H. Okawa, M. Shibata, and K. Kiuchi, *Phys. Rev. D* **83**, 124008 (2011).
- [30] K. Kiuchi, K. Kyutoku, Y. Sekiguchi, M. Shibata, and T. Wada, *Phys. Rev. D* **90**, 041502 (2014).
- [31] R. De Pietri, A. Feo, F. Maione, and F. Löffler, *Phys. Rev. D* **93**, 064047 (2016).
- [32] A. Endrizzi, R. Ciolfi, B. Giacomazzo, W. Kastaun, and T. Kawamura, *Classical and Quantum Gravity* **33**, 164001 (2016).
- [33] M. Hanauske, K. Takami, L. Bovard, L. Rezzolla, J. A. Font, F. Galeazzi, and H. Stöcker, *Phys. Rev. D* **96**, 043004 (2017).
- [34] R. Ciolfi, W. Kastaun, B. Giacomazzo, A. Endrizzi, D. M. Siegel, and R. Perna, *Phys. Rev. D* **95**, 063016 (2017).
- [35] M. Shibata and K. Kiuchi, *Phys. Rev. D* **95**, 123003 (2017).
- [36] D. Radice, A. Perego, S. Bernuzzi, and B. Zhang, *Mon. Not. R. Astron. Soc.* **481**, 3670 (2018).
- [37] D. Radice, A. Perego, K. Hotokezaka, S. A. Fromm, S. Bernuzzi, and L. F. Roberts, *Astrophys. J.* **869**, 130 (2018).
- [38] M. G. Alford, L. Bovard, M. Hanauske, L. Rezzolla, and K. Schwenzer, *Phys. Rev. Lett.* **120**, 041101 (2018).
- [39] A. Endrizzi, D. Logoteta, B. Giacomazzo, I. Bombaci, W. Kastaun, and R. Ciolfi, *Phys. Rev. D* **98**, 043015 (2018).
- [40] K. Kiuchi, K. Kyutoku, M. Shibata, and K. Taniguchi, *Astrophys. J.* **876**, L31 (2019).
- [41] R. De Pietri, A. Feo, J. A. Font, F. Löffler, M. Pasquali, and N. Stergioulas, *Phys. Rev. D* **101**, 064052 (2020).
- [42] L. Rezzolla and O. Zanotti, *Relativistic Hydrodynamics* (Oxford University Press, Oxford, UK, 2013).
- [43] Y. Lim and J. W. Holt, arXiv e-prints, arXiv:1909.09089 (2019).
- [44] J.-J. Lu, Z.-H. Li, G. F. Burgio, A. Figura, and H. J. Schulze, *Phys. Rev. C* **100**, 054335 (2019).
- [45] Z.-H. Li and H. J. Schulze, *Phys. Rev. C* **78**, 028801 (2008).
- [46] J.-B. Wei, J.-J. Lu, G. F. Burgio, Z.-H. Li, and H. J. Schulze, *European Physical Journal A* **56**, 63 (2020).
- [47] C. Bloch and C. De Dominicis, *Nuclear Physics* **7**, 459 (1958).
- [48] A. Lejeune, P. Grangé, M. Martzloff, and J. Cugnon, *Nuclear Physics A* **453**, 189 (1986).
- [49] M. Baldo, *Nuclear Methods and Nuclear Equation of State (International Review of Nuclear Physics)* (World Scientific Pub Co Inc (November 16, 1999), 1999).
- [50] M. Baldo and L. S. Ferreira, *Phys. Rev. C* **59**, 682 (1999).
- [51] O. E. Nicotra, M. Baldo, G. F. Burgio, and H. J. Schulze, *Astron. Astrophys.* **451**, 213 (2006).
- [52] O. E. Nicotra, M. Baldo, G. F. Burgio, and H. J. Schulze, *Phys. Rev. D* **74**, 123001 (2006).
- [53] A. Li, X. R. Zhou, G. F. Burgio, and H. J. Schulze, *Phys. Rev. C* **81**, 025806 (2010).
- [54] G. F. Burgio, H. J. Schulze, and A. Li, *Phys. Rev. C* **83**, 025804 (2011).
- [55] G. F. Burgio and H. J. Schulze, *Astron. Astrophys.* **518**, A17 (2010).
- [56] R. Wiringa, V. Stoks, and R. Schiavilla, *Phys. Rev. C* **51**, 38 (1995).
- [57] R. Machleidt, K. Holinde, and C. Elster, *Physics Reports* **149**, 1 (1987).
- [58] R. Machleidt, *Adv. Nucl. Phys.* **19**, 189 (1989).
- [59] M. M. Nagels, T. A. Rijken, and J. J. de Swart, *Phys. Rev. D* **17**, 768 (1978).
- [60] V. G. J. Stoks, R. A. M. Klomp, C. P. F. Terheggen, and J. J. de Swart, *Phys. Rev. C* **49**, 2950 (1994).
- [61] P. Grangé, A. Lejeune, M. Martzloff, and J.-F. Mathiot, *Phys. Rev. C* **40**, 1040 (1989).
- [62] W. Zuo, A. Lejeune, U. Lombardo, and J. F. Mathiot, *Nuclear Physics A* **706**, 418 (2002).
- [63] Z.-H. Li, U. Lombardo, H. J. Schulze, and W. Zuo, *Phys. Rev. C* **77**, 034316 (2008).
- [64] J. Carlson, V. Pandharipande, and R. Wiringa, *Nuclear Physics A* **401**, 59 (1983).
- [65] R. Schiavilla, V. Pandharipande, and R. Wiringa, *Nuclear Physics A* **449**, 219 (1986).
- [66] M. Baldo, I. Bombaci, and G. F. Burgio, *Astron. Astrophys.* **328**, 274 (1997).
- [67] X. R. Zhou, G. F. Burgio, U. Lombardo, H. J. Schulze, and W. Zuo, *Phys. Rev. C* **69**, 018801 (2004).
- [68] W. Zuo, Z. H. Li, A. Li, and G. C. Lu, *Phys. Rev. C* **69**, 064001 (2004).
- [69] I. Bombaci and U. Lombardo, *Phys. Rev. C* **44**, 1892 (1991).
- [70] W. Zuo, I. Bombaci, and U. Lombardo, *Phys. Rev. C* **60**, 024605 (1999).
- [71] J.-J. Lu, F. Li, Z.-H. Li, C.-Y. Chen, G. F. Burgio, and H. J. Schulze, arXiv e-prints, arXiv:2005.14583 (2020).
- [72] D. Radice, L. Rezzolla, and F. Galeazzi, *Class. Quantum Grav.* **31**, 075012 (2014).
- [73] H. T. Cromartie, E. Fonseca, S. M. Ransom, P. B. Demorest, Z. Arzoumanian, H. Blumer, P. R. Brook, M. E. DeCesar, T. Dolch, J. A. Ellis, R. D. Ferdman, E. C. Ferrara, N. Garver-Daniels, P. A. Gentile, M. L. Jones, M. T. Lam, D. R. Lorimer, R. S. Lynch, M. A. McLaughlin, C. Ng, D. J. Nice, T. T. Pennucci, R. Spiewak, I. H. Stairs, K. Stovall, J. K. Swiggum, and W. W. Zhu, *Nature Astronomy* **4**, 72 (2020).
- [74] M. C. Miller, F. K. Lamb, A. J. Dittmann, S. Bogdanov, Z. Arzoumanian, K. C. Gendreau, S. Guillot, A. K. Harding, W. C. G. Ho, J. M. Lattimer, R. M. Ludlam, S. Mahmoodifar, S. M. Morsink, P. S. Ray, T. E. Strohmayer, K. S. Wood, T. Enoto, R. Foster, T. Okajima, G. Prigozhin, and Y. Soong, *The Astrophysical Journal* **887**, L24 (2019).
- [75] T. E. Riley, A. L. Watts, S. Bogdanov, P. S. Ray, R. M. Ludlam, S. Guillot, Z. Arzoumanian, C. L. Baker, A. V. Bilous, D. Chakrabarty, K. C. Gendreau, A. K. Harding, W. C. G. Ho, J. M. Lattimer, S. M. Morsink, and T. E. Strohmayer, *Astrophys. J. Lett.* **887**, L21 (2019).
- [76] S. Koeppel, L. Bovard, and L. Rezzolla, *Astrophys. J. Lett.* **872**, L16 (2019).
- [77] A. Bauswein, S. Blacker, G. Lioutas, T. Soutanis, V. Vijayan, and N. Stergioulas, arXiv e-prints, arXiv:2010.04461 (2020).
- [78] E. T. Newman and R. Penrose, *J. Math. Phys.* **3**, 566 (1962), erratum in *J. Math. Phys.* **4**, 998 (1963).
- [79] J. N. Goldberg, A. J. MacFarlane, E. T. Newman, F. Rohrlich, and E. C. G. Sudarshan, *J. Math. Phys.* **8**, 2155 (1967).
- [80] C. Reisswig and D. Pollney, *Class. Quantum Grav.* **28**, 195015 (2011).
- [81] J. S. Read, L. Baiotti, J. D. E. Creighton, J. L. Friedman, B. Giacomazzo, K. Kyutoku, C. Markakis, L. Rezzolla, M. Shibata, and K. Taniguchi, *Phys. Rev. D* **88**, 044042 (2013).
- [82] K. Takami, L. Rezzolla, and L. Baiotti, *Phys. Rev. D* **91**, 064001 (2015).

- [83] L. J. Papenfort, R. Gold, and L. Rezzolla, *Phys. Rev. D* **98**, 104028 (2018).
- [84] LORENE, Langage Objet pour la Relativité Numérique, www.lorene.obspm.fr.
- [85] E.ourgoulhon, P. Grandclément, K. Taniguchi, J. A. Marck, and S. Bonazzola, *Phys. Rev. D* **63**, 064029 (2001).
- [86] D. Brown, P. Diener, O. Sarbach, E. Schnetter, and M. Tiglio, *Phys. Rev. D* **79**, 044023 (2009).
- [87] F. Loeffler, J. Faber, E. Bentivegna, T. Bode, P. Diener, R. Haas, I. Hinder, B. C. Mundim, C. D. Ott, E. Schnetter, G. Allen, M. Campanelli, and P. Laguna, *Class. Quantum Grav.* **29**, 115001 (2012).
- [88] H. O. Kreiss and J. Olinger, *Methods for the approximate solution of time dependent problems* (GARP publication series No. 10, Geneva, 1973).
- [89] D. Alic, C. Bona-Casas, C. Bona, L. Rezzolla, and C. Palenzuela, *Phys. Rev. D* **85**, 064040 (2012).
- [90] D. Alic, W. Kastaun, and L. Rezzolla, *Phys. Rev. D* **88**, 064049 (2013).
- [91] M. Bezares, C. Palenzuela, and C. Bona, *Phys. Rev. D* **95**, 124005 (2017).
- [92] M. Alcubierre, B. Brügmann, P. Diener, M. Koppitz, D. Pollney, E. Seidel, and R. Takahashi, *Phys. Rev. D* **67**, 084023 (2003).
- [93] D. Pollney *et al.*, *Phys. Rev. D* **76**, 124002 (2007).
- [94] D. Radice, L. Rezzolla, and F. Galeazzi, *Mon. Not. R. Astron. Soc. L.* **437**, L46 (2014).
- [95] D. Radice, L. Rezzolla, and F. Galeazzi, in *Numerical Modeling of Space Plasma Flows ASTRONUM-2014*, Astronomical Society of the Pacific Conference Series, Vol. 498, edited by N. V. Pogorelov, E. Audit, and G. P. Zank (2015) p. 121, [arXiv:1502.00551 \[gr-qc\]](https://arxiv.org/abs/1502.00551).
- [96] A. Suresh and H. T. Huynh, *Journal of Computational Physics* **136**, 83 (1997).
- [97] D. Radice and L. Rezzolla, *Astron. Astrophys.* **547**, A26 (2012).
- [98] E. Schnetter, S. H. Hawley, and I. Hawke, *Class. Quantum Grav.* **21**, 1465 (2004).
- [99] F. Galeazzi, W. Kastaun, L. Rezzolla, and J. A. Font, *Phys. Rev. D* **88**, 064009 (2013).
- [100] D. Radice, F. Galeazzi, J. Lippuner, L. F. Roberts, C. D. Ott, and L. Rezzolla, *Mon. Not. R. Astron. Soc.* **460**, 3255 (2016).
- [101] K. Kiuchi, K. Kyutoku, Y. Sekiguchi, and M. Shibata, *Phys. Rev. D* **97**, 124039 (2018).
- [102] S. Fujibayashi, Y. Sekiguchi, K. Kiuchi, and M. Shibata, *Astrophys. J.* **846**, 114 (2017).
- [103] stellarcollapse, (2017), <https://stellarcollapse.org/>.
- [104] R. Gill, A. Nathanail, and L. Rezzolla, *Astrophys. J.* **876**, 139 (2019).
- [105] S. Bernuzzi, M. Breschi, B. Daszuta, A. Endrizzi, D. Logoteta, V. Nedora, A. Perego, F. Schianchi, D. Radice, F. Zappa, I. Bombaci, and N. Ortiz, arXiv e-prints, arXiv:2003.06015 (2020).
- [106] W. Kastaun, R. Ciolfi, and B. Giacomazzo, *Phys. Rev. D* **94**, 044060 (2016).
- [107] S. Rosswog, M. Liebendörfer, F.-K. Thielemann, M. B. Davies, W. Benz, and T. Piran, *Astron. Astrophys.* **341**, 499 (1999).
- [108] L. Bovard, D. Martin, F. Guercilena, A. Arcones, L. Rezzolla, and O. Korobkin, *Phys. Rev. D* **96**, 124005 (2017).
- [109] M. Shibata and K. Kiuchi, *Phys. Rev. D* **95**, 123003 (2017).
- [110] D. Radice, *Astrophys. J. Lett.* **838**, L2 (2017).
- [111] LIGO Scientific Collaboration, Virgo Collaboration, Gamma-Ray Burst Monitor, INTEGRAL, B. P. Abbott, R. Abbott, T. D. Abbott, F. Acernese, K. Ackley, C. Adams, T. Adams, P. Addesso, R. X. Adhikari, V. B. Adya, and et al. (LIGO Scientific Collaboration and Virgo Collaboration), *Astrophys. J. Lett.* **848**, L13 (2017).
- [112] K. D. Kokkotas and B. G. Schmidt, *Living Rev. Relativ.* **2**, 2 (1999).
- [113] A. Bauswein, H.-T. Janka, K. Hebeler, and A. Schwenk, *Phys. Rev. D* **86**, 063001 (2012).
- [114] S. Vretinaris, N. Stergioulas, and A. Bauswein, *Phys. Rev. D* **101**, 084039 (2020).
- [115] A. Bauswein, R. Oechslin, and H.-T. Janka, *Phys. Rev. D* **81**, 024012 (2010).
- [116] S. Bernuzzi, arXiv e-prints, arXiv:2004.06419 (2020).
- [117] D. Radice and L. Dai, *European Physical Journal A* **55**, 50 (2019).
- [118] K. Hotokezaka and T. Piran, *Mon. Not. R. Astron. Soc.* **450**, 1430 (2015).
- [119] T. Vincent, F. Foucart, M. D. Duez, R. Haas, L. E. Kidder, H. P. Pfeiffer, and M. A. Scheel, *Phys. Rev. D* **101**, 044053 (2020).
- [120] J. Lippuner and L. F. Roberts, *Astrophys. J.* **815**, 82 (2015).
- [121] B. D. Metzger, *Living Reviews in Relativity* **20**, 3 (2017).